

Effects of geometric shape of LWSCR (lazy-wave steel catenary riser) on its global performance and structural behavior

Seungjun Kim^{*1} and Moo-Hyun Kim^{2a}

¹Department of Construction Safety and Disaster Prevention Engineering, Daejeon University,
62 Daehak-ro, Dong-gu, Daejeon 34520, Republic of Korea

²Department of Ocean Engineering, Texas A&M University, 3136 TAMU, College Station, TX 77843, USA

(Received July 9, 2018, Revised August 20, 2018, Accepted August 22, 2018)

Abstract. This study aims to investigate the behavioral characteristics of the LWSCR (lazy-wave steel catenary riser) for a turret-moored FPSO (Floating Production Storage Offloading) by using fully-coupled hull-mooring-riser dynamic simulation program in time domain. In particular, the effects of initial geometric profile on the global performance and structural behavior are investigated in depth to have an insight for optimal design. In this regard, a systematic parametric study with varying the initial curvature of sag and arch bend and initial position of touch down point (TDP) is conducted for 100-yr wind-wave-current (WWC) hurricane condition. The FPSO motions, riser dynamics, constituent structural stress results, accumulated fatigue damage of the LWSCR are presented and analyzed to draw a general trend of the relationship between the LWSCR geometric parameters and the resulting dynamic/structural performance. According to this study, the initial curvature of the sag and arch bend plays an important role in absorbing transferred platform motions, while the position of TDP mainly affects the change of static-stress level.

Keywords: steel catenary riser; lazy-wave steel catenary riser; turret-moored FPSO; hull/mooring/riser coupled dynamic analysis; global dynamics; time-domain simulation; curvature; TDP; internal stress; fatigue; optimal design

1. Introduction

A turret-moored FPSO is one of the most widely used floating system for producing offshore oil and gas resources in deep water because of their advantages in huge storage capacity, ample deck space giving better layout flexibility, cost efficiency for short-life field, mobility, and no necessary of pipelines to onshore. Also, for production riser, steel catenary risers (SCRs) have been widely used due to its low cost and structural simplicity. However, it is also well known that the conventional SCRs should be very carefully designed for FPSO or semisubmersibles due to their potentially large downward motions that can cause temporary local dynamic buckling near SCR's TDP (touch-down point). Even if no dynamic buckling occurs, risers' large dynamic motions significantly reduce fatigue life.

When a floating platform is excited by hurricane waves, the induced large platform motions

*Corresponding author, Assistant Professor, E-mail: skim@dju.kr

^a Professor, E-mail: m-kim3@tamu.edu

directly affect the attached mooring lines and risers. The induced dynamic responses of the risers in turn cause significant internal-stress amplification. Also, when unacceptably large downward heave motions occur, the resulting compressional force (negative tension) can cause local dynamic buckling near touch-down zone. This is why SCRs are rarely used for FPSOs in hurricane conditions. Kuiper *et al.* (2008) investigated the mechanism of the localized dynamic buckling of top-tensioned risers due to heave motions of a TLP. Kim *et al.* (2014) and Kim and Kim (2015) also investigated the local dynamic buckling of deep-water SCRs due to large heave/pitch motions of a FPSO. Even without the occurrence of local dynamic buckling in lesser sea environments, large motion-induced dynamic stresses of SCRs are a great concern for fatigue damage. Usually, excessive structural stresses may occur at hang-off and touchdown zone. In this regard, several researchers have claimed that the conventional SCRs may not be appropriate for semisubmersibles or turret-moored FPSOs in the GOM (Gulf of Mexico) or North Sea (Wu and Huang 2007, Yue *et al.* 2010, Yue *et al.* 2011, Yang and Li 2011).

To circumvent the above problems of SCR, lazy-wave steel catenary risers (LWSCRs) are introduced for the application of turret-moored FPSOs in GOM or North Sea. The LWSCR is more expensive and more difficult to design but it is supposed to have excellent motion-absorption effect, which can avoid local dynamic buckling near TDP and also significantly increase fatigue life. In case of LWSCR, by using additional buoyancy modules in a specific region of the riser, intermediate arch and sag parts can be made within the configuration. Because of the intermediate region, the motion of the riser can be effectively isolated from the motion of the floater. As a result, LWSCRs may avoid many potential behavioral problems that conventional SCRs may suffer (Jacob *et al.* 1999, Silva *et al.* 1999, Torres *et al.* 2001, Torres *et al.* 2002, Torres *et al.* 2003, Li and Nguyen 2010, Kim *et al.* 2014). However, as an unavoidable disadvantage, LWSCRs may have flow-assurance problems when its curvature is large.

Using a simplified approach, Yue *et al.* (2011) performed a comparative study to compare dynamic performance of conventional SCR, shaped SCR, and LWSCR, which are attached to the same turret moored FPSO in 800 m water depth, West Africa. In the study, it was shown that LWSCR shows better structural performance than other compared risers. Using another simplified approach, Yang and Li (2011) also studied the fatigue life of deep-water LWSCRs. Authors (Kim and Kim 2015) investigated the global performance and structural efficiency of an SCR and LWSCR for a turret-moored FPSO by using fully-coupled hull-mooring-riser time-domain dynamic analysis program developed by the 2nd author's lab during the past two decades.

In this paper, the dynamic behavior of deep-water LWSCRs for a turret-moored FPSO is investigated in detail with varying important design parameters. By performing the fully-coupled hull-mooring-riser dynamic analysis, riser dynamics, distribution of internal stress along the riser, and accumulated fatigue damage are numerically simulated to investigate design preferences and optimization. In this regard, two case studies are conducted with varying initial curvature and initial position of TDP. The detailed findings are summarized in the discussion and conclusion sections.

2. General configuration of LWSCR (lazy wave steel catenary riser)

The initial configuration of LWSCR can be expressed by three individual catenaries, hangoff catenary, buoyancy catenary, and touchdown catenary, as shown in Fig. 1 (Li *et al.* 2010, Kim and Kim 2015). The catenaries are given by the following equations defined with individual origins

and local coordinates, x-y, u-v, and p-q

$$y = a_i(\cosh x / a_i - D) \tag{1}$$

$$v = a_j(\cosh u / a_j - D) \tag{2}$$

$$q = a_k(\cosh p / a_k - D) \tag{3}$$

The equations contain the unknowns $\alpha_{i,j,k}$, curvature radius at each origin of the catenaries. So, the initial shape of the LWSCR can simply be expressed by the equation if the unknowns are defined.

By the force equilibrium condition between the segments in hanging part shown in Fig. 2, the relation between the wet weights per unit length of each catenary $Q_{i,j,k}$, segment length $S_{i,j,k}$, and the initial curvature radius $a_{i,j,k}$ can be obtained as well as the general conditions of the conventional catenary members shown in Table 1.

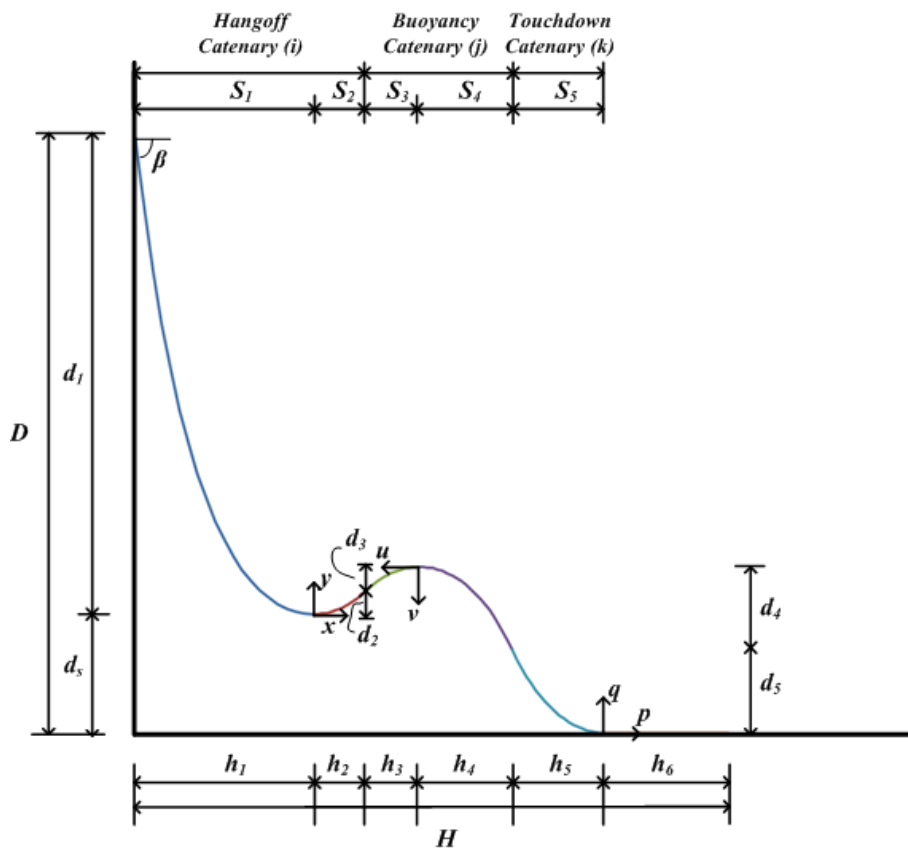


Fig. 1 General configuration of LWSCR (Kim and Kim 2015)

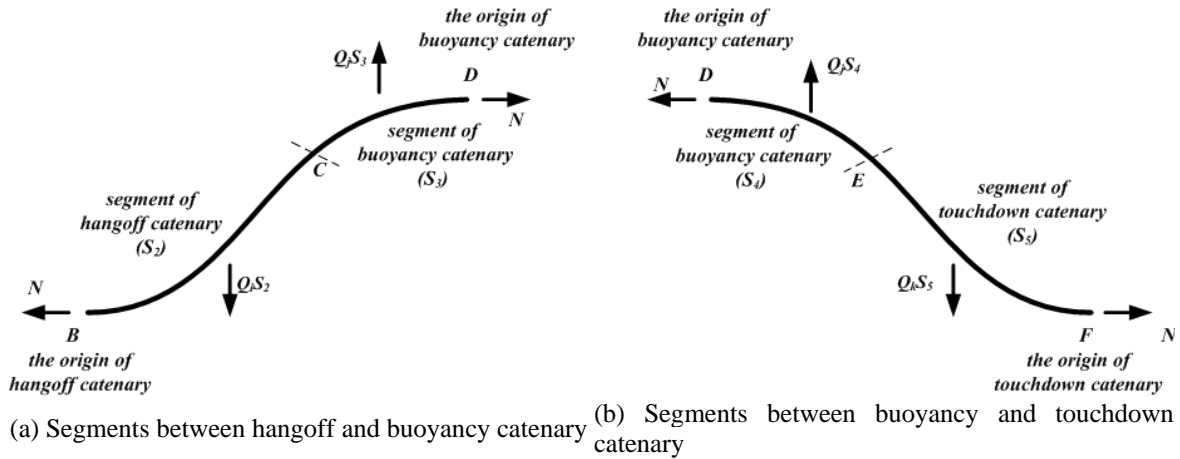


Fig. 2 Static force equilibrium between segment S_2, S_3, S_4 and S_5

Table 1 General condition of conventional catenary members

Arc length of a catenary from its origin, $S(x)$	$S(x) = a \sinh(x/a)$	(4)
Inclination angle, $\beta(x)$	$\beta = \tan^{-1}(S(x)/a)$	(5)
Horizontal force induced by effective weight, $N(x)$	$N(x) = T(x) \cos \beta = aQ$ (const)	(6)
Tensile force induced by effective weight, $T(x)$	$T(x) = N(x) / \cos \beta = aQ / \cos \beta$	(7)

First of all, following equations can be written by the vertical force equilibrium condition at each part shown in Fig. 2

$$Q_i S_2 = Q_j S_3 \tag{8}$$

$$Q_j S_4 = Q_k S_5 \tag{9}$$

Further, by the general relationship between the constant horizontal force N , $a_{i,j,k}$ and $Q_{i,j,k}$, following relationship can be expressed

$$\frac{Q_j}{Q_i} = \frac{S_2}{S_3} = \frac{a_i}{a_j} \tag{10}$$

$$\frac{Q_k}{Q_j} = \frac{S_4}{S_5} = \frac{a_j}{a_k} \tag{11}$$

By using Eqs. (10) and (11) with general relationships of catenary shown in Eqs. (4)-(7), the initial shape of the LWSCR can be easily expressed with exact magnitude and location of required additional buoyancy forces which should be applied to the buoyancy catenary.

3. Hull/Mooring/Riser coupled dynamic analysis

To reasonably investigate the dynamic behavior of deep-water riser with FPSO, nonlinear hull/mooring/risers coupled dynamic analysis should be performed. In this section, a brief summary of methodology is explained as follows. The time-domain hull/mooring/riser coupled dynamic simulation program CHARM3D (Ran and Kim 1997, Ran 2000, Tahar and Kim 2003, Yang and Kim 2010, 2011, Kang and Kim 2012, Kim and Kim 2015) has extensively been developed in the 2nd author's lab during the past two decades. The computer program has also been extensively verified against numerous experimental and field measurements.

For static or dynamic analysis of mooring lines and risers, an extension of the rod FE (finite element) theory developed by Garrett (1982) was used. Using long slender elastic rod element without twisting moment, the following linear momentum conservation equation can be derived with respect to a position vector $\vec{r}(s,t)$, a function of arc length s and time t

$$-(B\vec{r}''')'' + (\lambda\vec{r}')' + \vec{q} = m\ddot{\vec{r}} \quad (12)$$

$$\lambda = T - B\kappa^2 \quad (13)$$

where primes and dots denote spatial s -derivative and time derivative, respectively, B is the bending stiffness, T is the local effective tension, κ is the local curvature, m is the mass per unit length, and \vec{q} is the distributed force on the rod per unit length. In Eq. (13), the scalar variable λ can be regarded as a Lagrange multiplier. Assuming the rod is elastically extensible, the following condition can be applied

$$\frac{1}{2}(\vec{r} \cdot \vec{r} - l) = \frac{T}{A_t E} \approx \frac{\lambda}{A_t E} \quad (14)$$

where E is Young's modulus, and A_t is effective sectional area (=outer – inner cross sectional area). In this study, geometric nonlinearity is fully considered using generalized coordinate and there is no special assumption made concerning the shape or orientation of lines. High-order FE are used for geometric and force variations along each member.

For a normal component q_n of the distributed external force acting on the rod per unit length, the following equation is used based on the equation of generalized Morison equation

$$q_n = C_I \rho A_e \dot{v}_n + C_D \frac{1}{2} \rho D |v_{nr}| v_{nr} + C_m \rho A_e \ddot{r}_n \quad (15)$$

where C_I , C_D and C_m are inertia, drag, and added mass coefficients, and \dot{v}_n , v_{nr} , and \ddot{r}_n are normal fluid acceleration, normal relative velocity, and normal structure acceleration, respectively. Also, ρ , D and A_e in the equation are fluid density, outer diameter, and outer cross sectional area, respectively. Further, the effective weight or net buoyancy of the rod should be included in q_n , as a static load.

The upper ends of mooring lines and risers are connected to the hull fairlead through generalized elastic springs and dampers. At the connection points, the forces proportional to the relative displacements are transmitted to the hull. The transmitted forces from mooring lines and risers to the platform are given by

$$\tilde{F}_p = \tilde{K}(\tilde{T}\tilde{u}_p - \tilde{u}_I) + \tilde{C}(\tilde{T}\dot{\tilde{u}}_p - \dot{\tilde{u}}_I) \tag{16}$$

where \tilde{K}, \tilde{C} are stiffness and damping matrices of connectors at the connection point, and \tilde{T} represents a transformation matrix between the platform origin and connection point. Also, \tilde{u}_p and \tilde{u}_I denote column matrices for the displacements of the platform and connection point, respectively.

Then, the following hull response equation is combined into the riser/mooring equation in the time domain

$$(\tilde{M} + \tilde{M}_a(\infty))\ddot{\tilde{u}}_p + \int_0^\infty \tilde{R}(t-\tau)\dot{\tilde{u}}_p d\tau + \tilde{K}_H\tilde{u}_p = \tilde{F}_D + \tilde{F}^{(1)} + \tilde{F}^{(2)} + \tilde{F}_p + \tilde{F}_w + \tilde{F}_c + \tilde{F}_{WD} \tag{17}$$

where \tilde{M}, \tilde{M}_a = mass and added mass matrix, \tilde{R} = retardation function (inverse cosine Fourier transform of radiation damping) matrix, \tilde{K}_H = hydrostatic restoring coefficient, \tilde{F}_D = drag force matrix on the hull, $\tilde{F}^{(1)}, \tilde{F}^{(2)}$ = first- and second-order wave load matrix on the hull, \tilde{F}_p = transmitted force matrix from the interface, \tilde{F}_w = dynamic wind loading, \tilde{F}_c = current loading on hull, and \tilde{F}_{WD} = wave drift damping force matrix. More details of the methodology about finite element formulation, solving scheme about coupled static/dynamic problems in time domain are given in Refs. (Ran and Kim 1997, Ran 2000)

When analyzing risers, the interaction between the riser and seabed should be considered. For the interaction, the seabed is basically modeled as a quadratic elastic spring in vertical direction. In addition, the lateral and longitudinal friction effects are considered by the Coulomb friction model as shown in Fig. 3(a). In this study, a value of 0.25 is selected as the dynamic friction factor μ . The normal force R for friction is mainly the net weight of riser compensated by instantaneous vertical inertia forces.

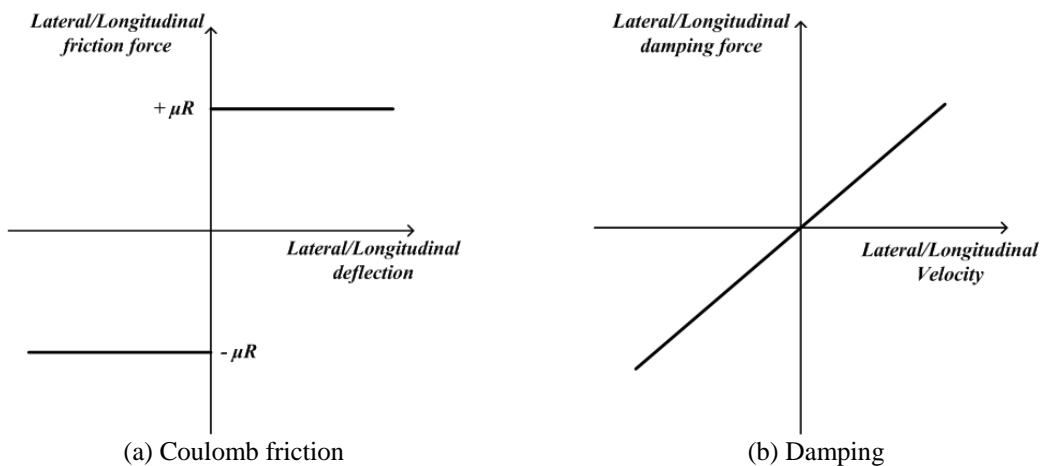


Fig. 3 Model for lateral and longitudinal interactions between riser and seabed

Table 2 Main particulars of the vessel (Tahar and Kim 2003)

Designation	Symbol	Unit	Quality
Production level		<i>bpd</i>	120,000
Storage		<i>bbls</i>	1,440,000
Vessel size		<i>kDWT</i>	200.0
Length between perpendicular	L_{pp}	<i>m</i>	310.00
Breadth	B	<i>m</i>	47.17
Depth	H	<i>m</i>	28.04
Draft	T	<i>m</i>	18.9
Displacement		<i>MT</i>	240,869
Length-beam ratio	L / B		6.57
Beam-draft ratio	B / T		2.5
Block coefficient	C_b		0.85
Center of buoyancy Forward section10	FB	<i>m</i>	6.6
Center of gravity above Base	KG	<i>m</i>	13.3
Water plane area	A	m^2	13,400
Frontal wind area	A_f	m^2	1011.7
Transverse wind area	A_b	m^2	3771.9
Roll radius of gyration at CG	R_{xx}	<i>m</i>	14.77
Pitch radius of gyration at CG	R_{yy}	<i>m</i>	77.47
Yaw radius of gyration CG	R_{zz}	<i>m</i>	79.30
Turret in center line behind Fpp (20.5% Lpp)	X_{tur}	<i>m</i>	63.55
Turret elevation below tanker base	Z_{tur}	<i>m</i>	1.52
Turret Diameter		<i>m</i>	15.85

4. Dynamic behavior of deep-water LWSCR connected to the FPSO under harsh environmental condition

Basically, the dynamic behavior of risers is mainly affected by the motion of floating platform induced by the environmental sources. In this section, the dynamic characteristics of the LWSCR attached to the turret-moored FPSO are studied by hull/mooring/riser coupled dynamic analysis.

4.1 Analysis models

4.1.1 FPSO model

The FPSO model used in this study is a 200,000 DWT tanker moored in 1,829 m (6,000-ft) water depth, by a taut chain-polyester-chain mooring system with turret. The vessel was used in the previous studies conducted by Tahar and Kim (2003) and Kim and Kim (2015). The main particulars of the vessel are summarized in Table 2.

To obtain the hydrodynamic coefficients (added mass and radiation damping) and first- and second-order wave forces, WAMIT, a well-known second-order diffraction/radiation panel program is used. To use WAMIT for obtaining the required hydrodynamic coefficients and forces, the wetted surface of the FPSO at mean position should be discretized by 1,831 quadrilateral element panels as shown in Fig. 4. The discretization was determined after checking convergence with increasing panel numbers.

4.1.2 mooring system and riser model

Fig. 5 shows general arrangement of chain-polyester-chain mooring system and risers. The mooring system consists of 12 mooring lines arranged in four groups, as shown in Fig. 5(a). Each group is 90-degree apart and consists of 3 legs with 5 degrees apart. Also, 13 catenary risers are considered in this study as shown in Fig. 5(b). The main particulars of mooring system and risers are shown in Tables 2 and 3, respectively.

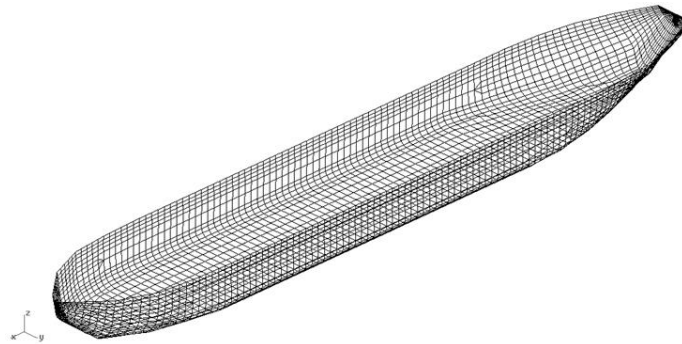
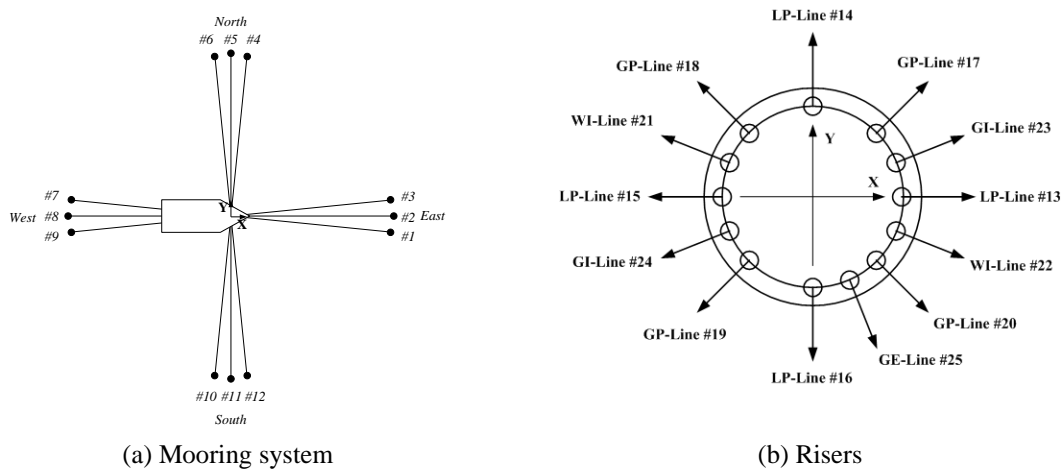


Fig. 4 Panel model of the wet surface of FPSO



(a) Mooring system

(b) Risers

Fig. 5 General arrangement of mooring system and risers

Table 2 Main particular of FPSO mooring system

Designation	Unit	Value
Water depth	m	1829
Pre-tension	kN	1424
Number of lines		4 × 3
Degree between the 3 lines	deg.	5
Length of mooring line	m	2652
Radius of location of chain stoppers on turn table	m	7.0
Segment 1(ground section): Chain		
Length at anchor point	m	121.9
Diameter	cm	9.52
Dry weight	N/m	1856
Weight in water	N/m	1615
Stiffness AE	kN	912081
Mean breaking load (MBL)	kN	7553
Segment 2: Polyester Rope		
Length	m	2438
Diameter	cm	16.0
Dry weight	N/m	168.7
Weight in water	N/m	44.1
Stiffness AE	kN	186825
Mean breaking load (MBL)	kN	7429
Segment 3(ground section): Chain		
Length at anchor point	m	91.4

Fig. 6 shows the numerical model for the turret-moored FPSO system used in this study. In this study, it is assumed that all the collinear environmental loadings come from west to east of the system for simplicity. In order to observe the dynamic response of the LWSCR under very harsh condition, LP-line #13 and #15, which align with the direction of the environmental loadings, are designed as the LWSCR while remaining production risers are designed as conventional SCR. Fig. 7 shows the initial configuration of the risers for the LP lines #13 and #15 and Table 4 shows the initial location of the TDP and anchor point of the risers. For each LWSCR, 128 high-order elements are used after checking the convergence.

Table 3 Main particular of risers

Designation	OD (m)	t (m)	EA (kN)	EI (kN·m ²)	Weight		C _{dn}
					dry (kg/m)	wet (kg/m)	
Liquid production risers	0.254	0.023	3.34E+06	2.25E+04	133.6	98.6	1
Gas production risers	0.386	0.018	4.16E+06	7.06E+04	166.5	46.6	1
Water injection risers	0.531	0.018	5.80E+06	1.91E+05	232.1	197.6	1.414
Gas injection risers	0.287	0.020	3.36E+06	3.01E+04	134.2	67.9	1.414
Gas export risers	0.343	0.017	3.48E+06	4.64E+04	139.3	44.6	1

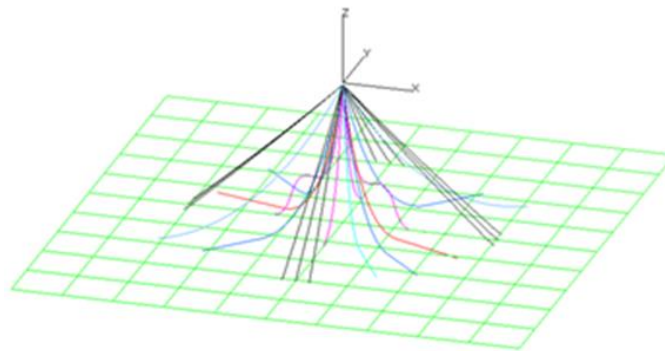


Fig. 6 Numerical model of the considered hull/mooring/riser system

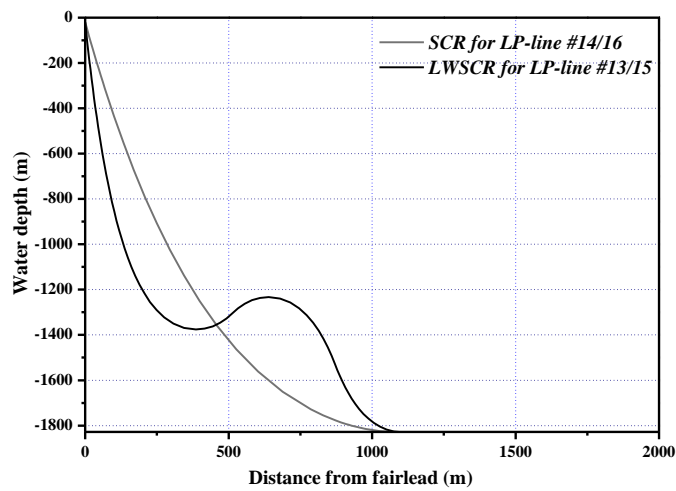


Fig. 7 Initial configuration of considered risers for LP #13 and #15

Table 4 Location of TDP and anchor point of risers

Risers for LP-line #13 and #15	TDP (m)	anchor (m)
SCR	1,095.68	1,905.80
LWSCR	1,118.75	1,922.55

(*for LWSCR, $d_1 = 0.75D$, $h_1 / H_{TDP} = 0.35$, and $H_{TDP} / H_{ANCHOR} = 0.58$ where d_1 : depth of first catenary segment, D : vertical distance between fairlead and seabed, h_1 : horizontal distances between the fairlead and the origin of sag bend, H_{TDP} : TDP horizontal distances between the fairlead and the TDP, H_{ANCHOR} : TDP horizontal distances between the fairlead and the anchor point)

To model the LWSCR with the desired initial shape, the buoyancy catenary is subjected to the additional buoyancy force of twice of wet weight per unit length induced by buoy modules. Using the equations for initial shape of the LWSCR, as described in the previous section, the magnitude and applied location of the additional buoyancy forces can exactly be calculated and defined. In CHARM3D, the force can be applied as the static concentrated force to find the static equilibrium profile in the static-analysis stage.

The time-domain simulation results for a similar FPSO system were extensively verified against model-testing results at the OTRC 3D wave basin at Texas A&M University (Kim *et al.* 2005).

4.2 Environmental condition

In this study, a typical 100-yr hurricane in the Gulf of Mexico with significant wave height of 15.79 m and peak wave period of 15.4 s is selected as the wave environment. To generate long crested irregular random waves without signal repetition, random perturbation of frequency interval was used. As input wave spectrum, the JONSWAP spectrum is used with enhancement parameter $\gamma = 2.4$. Also, for wind, 1 h mean wind speed of 48.01 m/s at 10-m altitude is used and the time dependent wind velocity is generated for 3 hours from the corresponding API wind spectrum. In this study, it is assumed that wind, wave, and current are propagating to the same direction, thus only collinear case with heading angle of 180° is considered for simplicity. Under the environmental condition, the dynamic behavior of LP-line #13 shown in Fig. 8(b) is mainly observed. A typical storm-induced steady shear current profile in the GOM with decreasing velocity with depth is given as the input current condition. Table 5 shows the summary of the 100-yr hurricane event.

Fig. 8 shows the 3-hour time history and regenerated spectrum of the random wave. Also shown is the input theoretical JONSWAP spectrum. Fig. 9 shows the time series and spectrum of dynamic wind speed at the height of 10 m above sea level, obtained by the equation of the 1-point wind spectrum of API Bulletin 2INT-MET (API, 2007). In both wave and wind cases, the regenerated spectra agree well with the respective input spectra warranting the correctness of the generated time series.

$$S(f) = \frac{320 \left(\frac{U_0}{10} \right)^2 \left(\frac{z}{10} \right)^{0.45}}{\left(1 + \tilde{f}^n \right)^{(5/3n)}} \quad (18)$$

Table 5 Environmental Conditions

Designation	Unit	Value
<i>Waves</i>		
H_s	m	15.79
T_p	sec.	15.40
Wave spectrum	JONSWAP ($\gamma = 2.4$)	
Wave direction	deg.	0° (to East)
<i>Wind</i>		
Wind speed (1-hr)		48.01
Wind spectrum	API Bulletin 2INT-MET	
Wind direction	deg.	0° (to East)
<i>Current profile</i>		
Depth: 0.0 m	m/s	2.41
50.4 m	m/s	1.80
100.8 m	m/s	0.0
2000.0 m	m/s	0.0
Current direction	deg.	0° (to East)

$$\tilde{f} = 172 f \left(\frac{z}{10} \right)^{2/3} \left(\frac{U_0}{10} \right)^{-0.75} \tag{19}$$

where $n = 0.468$ and where:

- $S(f)(m^2 s^{-2} / Hz)$: the spectral energy density at frequency f (Hz)
- $z(m)$: the height above sea level
- $U_0(m/s)$: the 1-hour mean wind speed at 10m above sea level

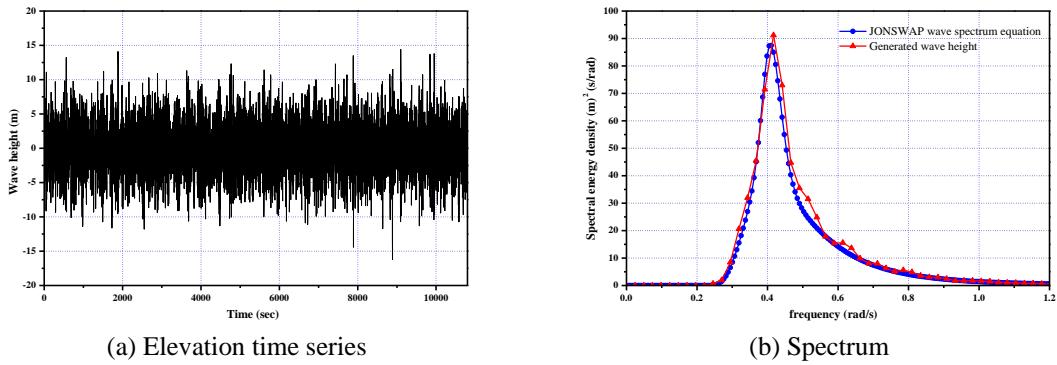


Fig. 8 Wave-elevation time series and spectrum

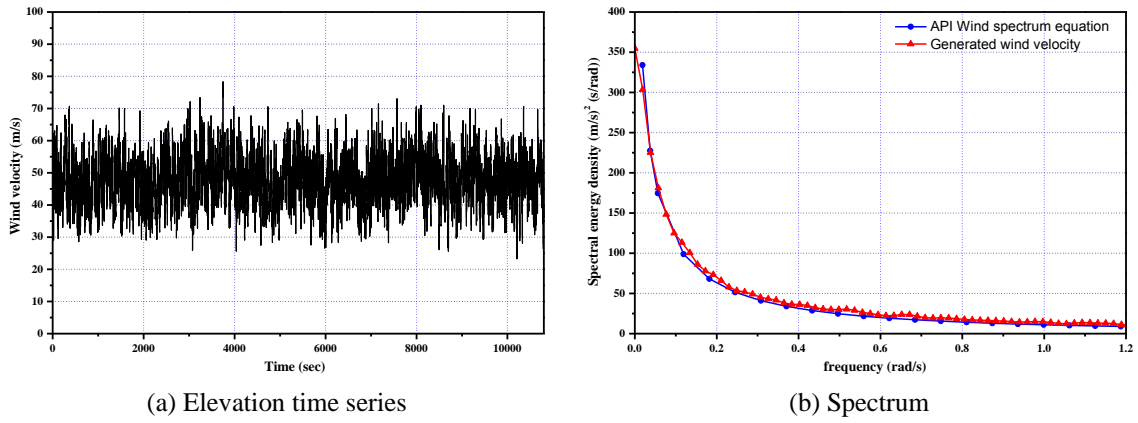


Fig. 9 wind-speed time series and spectrum (10m height)

4.3 Vessel motion

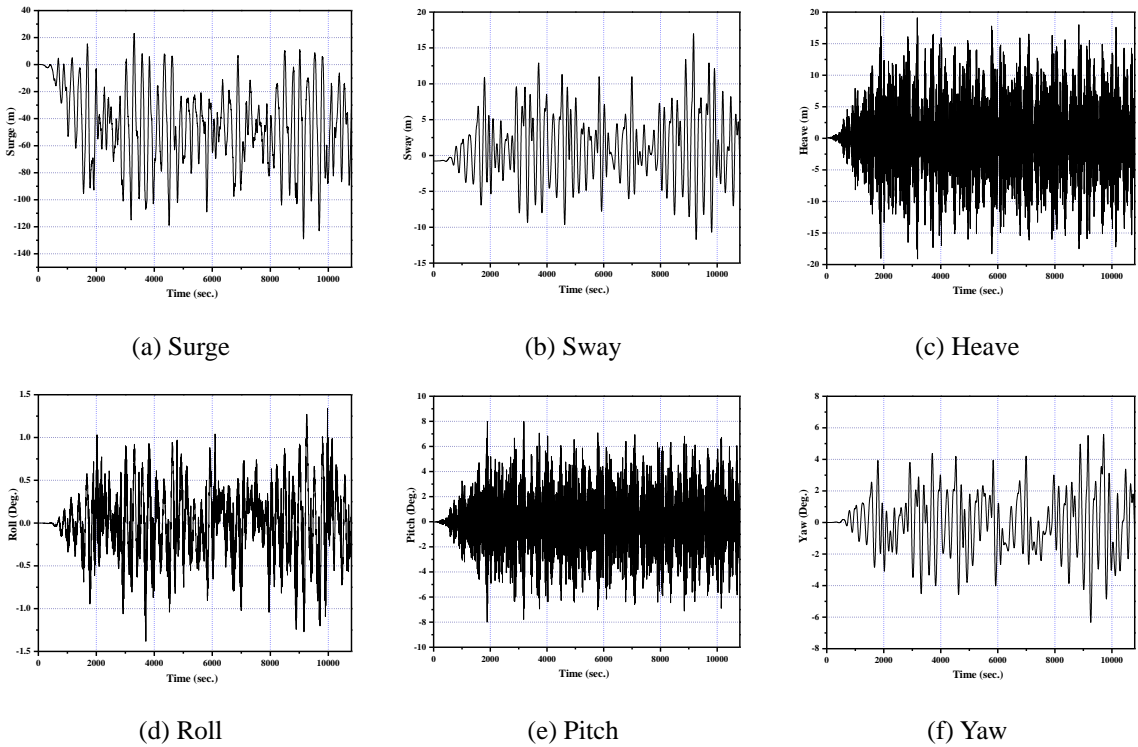


Fig. 10 6DOF Motions of the FPSO with LWSCRs (LP-line #13 and 15)

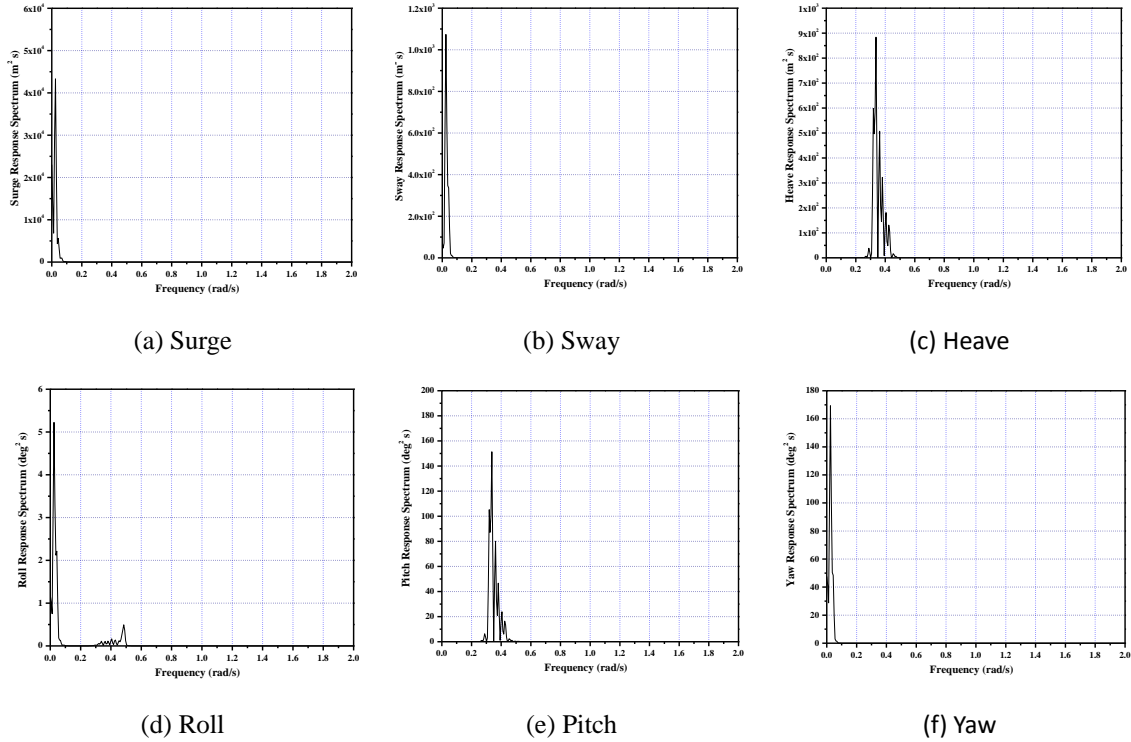


Fig. 11 Response spectra of the 6DOF motions

Table 6 Statistics of the vessel motions

	Max.	Min.	Mean	Standard Deviation
Surge (m)	23.029	-128.559	-47.281	28.584
Sway (m)	16.948	-11.859	1.182	4.767
Heave (m)	19.558	-19.261	0.019	6.239
Roll (deg)	1.344	-1.381	0.005	0.401
Pitch (deg)	8.071	-8.066	0.003	2.513
Yaw (deg)	5.555	-6.387	-0.032	2.002

By performing hull-mooring-riser coupled dynamic analysis in time-domain, the 6DOF motions of the floater, mooring and riser dynamics and the corresponding internal forces can be obtained under the specified environmental condition. Figs. 10 and 11 show the 6DOF-motion time series and spectra. The coordinate origin is located at the turret and on MWL with z vertically

upward, as shown in Fig. 5. The results successfully reproduce the general trend of such FPSO system characterized by slow-varying surge, sway, and yaw motions and wave-frequency heave, pitch, and roll motions. As shown in the figures, the heave and pitch motions at wave frequencies significantly contribute to riser dynamics (Kim and Kim 2015) i.e., the dynamic responses of mooring lines and risers are mainly affected by the heave and pitch motions, while the slowly-varying components mainly affect to the quasi-static response of the members.

4.4 Vessel motion

After performing the hull-mooring-riser coupled dynamic analysis using CHARM3D, the time-series of the riser dynamics are obtained. Fig. 12 represents the maximum, minimum, and mean vertical velocity at each node along the LP line #13. The motion isolation effect by having the buoyant reverse curvature is clearly shown in the result. The portion nearby the fairlead exhibits the maximum vertical velocity similar to that of FPSO turret. However, the vertical velocity is significantly reduced when reaching close to the sag. Because of the motion isolation effect by the intermediate sag and arch, the riser members beyond the buoyancy catenary are rarely affected by the vertical responses of FPSO even under the harsh environmental loadings.

The motion isolation effect can also be noticed in the vertical-displacement spectrum in Fig. 13. The significant reduction in the wave-frequency range is particularly noticeable. The increases of displacements at low frequency in Fig. 13 do not contribute to the increases of velocities, as shown in Fig. 14, so do not impose any engineering problems. Because the excitations by the FPSO rarely affect the dynamic behaviors of the LWSCR near TDP, the LWSCR is free of local dynamic buckling (Kim and Kim 2015) that can occur near TDP in the case of ordinary SCR. So, LWSCR is much safer than SCR in the most severe environmental conditions. By the same reason, the fatigue damage accumulation for the members nearby TDP is also greatly reduced.

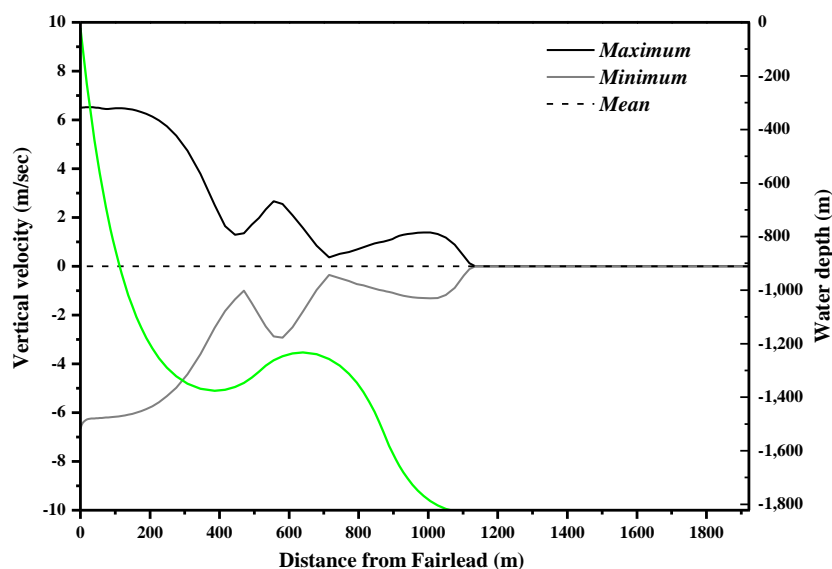


Fig. 12 Vertical velocity envelope of LWSCR

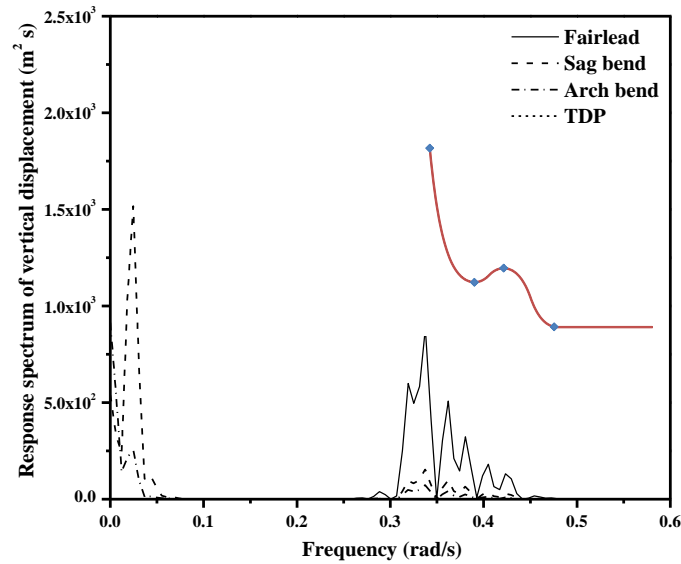


Fig. 13 Response spectra of vertical displacements of LWSCR

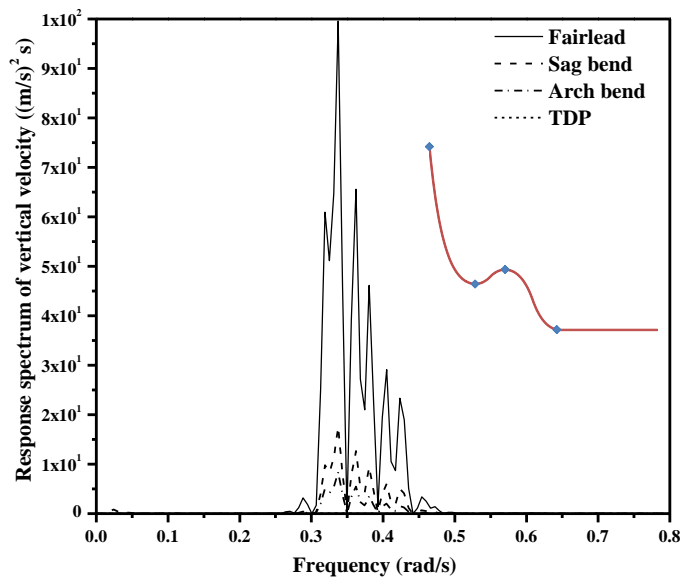


Fig. 14 Response spectra of vertical velocities of LWSCR

4.5 Internal forces on the risers

Fig. 15 exhibits the distribution of axial force and bending moment of the LWSCR. In the figures, maximum, minimum, and mean values of the force components are plotted to clearly observe their variation range. The axial force initially shows the monotonic decrease with depth due to the decrease of weight below. According to the general static characteristic of catenary, the

tensile force acting to each section is distributed proportion to $1/\cos \theta$ (θ =horizontally inclined angle). Therefore, the shape of the force distribution is similar to the shape of the catenary. In the buoyancy catenary region, the force distribution is opposite to the shape of the riser because the effective weight is applied to upper direction and the configuration is defined with the reversed origin (see Fig. 1). The maximum tension force should occur at the hang-off point as shown in the numerical result. Engineers do not want to use ordinary SCR in case of FPSO due to the possibility of local dynamic buckling near TDP caused by large vertical downward motions at the fairlead and the corresponding compressional forces. However, in the case of LWSCR, due to the motion isolation effect, no such serious problem is anticipated even in the harshest environments, which can be seen in that there is no negative tension along the LWSCR, especially near TDP. However, it was observed that the neighboring SCR suffered from the local dynamic buckling, which was analyzed in depth in Kim and Kim (2015).

In Fig. 15(b), maximum bending moment occurs at the maximum curvature of sag and arch bend, and TDP, which is mainly due to the static profile and the effects of dynamics are less important. It can simply be expected that more curvature will result in larger initial bending moment. More sag and arch curvatures also cause serious clogging problems for internal-fluid flows. In next section, the effect of the initial shape of sag and arch is investigated in detail.

In case of LWSCR, the numerical results show that no local dynamic buckling occurs due to the motion-isolation effect and the internal-force variations are acceptable. So, it can be concluded that LWSCR can be used for FPSO even in the harshest environments despite that the design becomes more difficult and cost is significantly increased compared to ordinary SCRs. Also, less dynamics mean less problems for fatigue damage.

4.6 Stress resultants

Internal forces acting on a section of riser can be classified into: axial force, major/minor axis bending moment, torsional moment, and shear force. Using the internal force components, the total stress can be calculated as follows

$$\text{Normal stress } \sigma_n = \frac{P}{A} \pm \frac{M_x}{I_x} y \mp \frac{M_y}{I_y} x \tag{20}$$

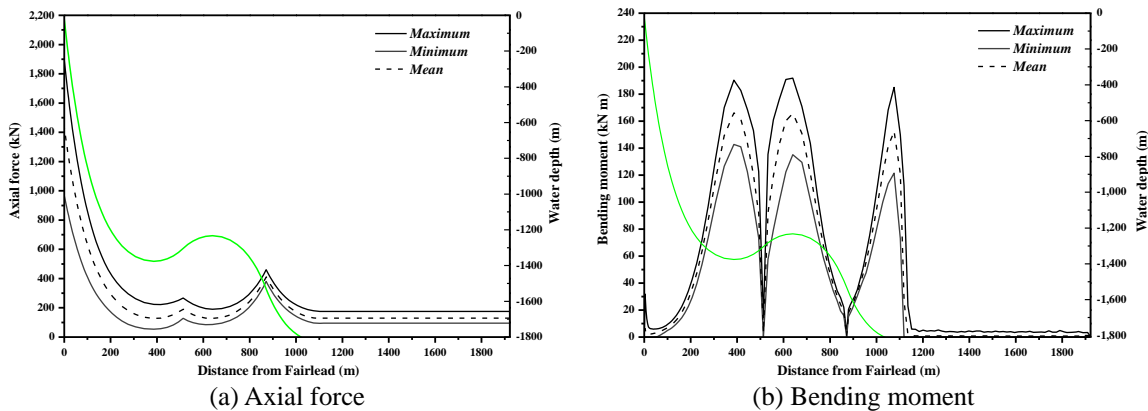


Fig. 15 Internal force distribution of the LWSCR

$$\text{Shear stress } \tau \equiv \frac{V_y \sin \theta_y}{\pi r_c t} \pm \frac{V_x \sin \theta_x}{\pi r_c t} \tag{21}$$

(Here, shear stress due to torsional moment is ignored because there is no significant torsional moment on a very slender and long riser)

In addition, internal and external pressures make hoop and radial stresses in the wall of riser as follows

$$\text{Hoop stress } \sigma_\theta = (p_i - p_e) \frac{D_o}{2t} - p_i \tag{22}$$

$$\text{Radial stress } \sigma_r = -\frac{(p_e D_o + p_i D_i)}{D_o + D_i} \tag{23}$$

where, p_i : internal pressure p_e : external pressure
 D_i : inner diameter D_o : outer diameter
 t : wall thickness

(API, 2009)

Using the stress components, Von-Mises stress can be calculated in order to check the final stress against yield stress. API RP 2nd (API, 2009) suggests following condition for material yield criteria.

$$\sigma_v \leq c_f \sigma_a = c_f c_a \sigma_y \tag{24}$$

where, σ_v : Von-mises stress
 c_f : design case factor (for extreme environmental condition, 1.2)
 c_a : allowable stress factor, 2/3
 σ_y : minimum yield stress of a material

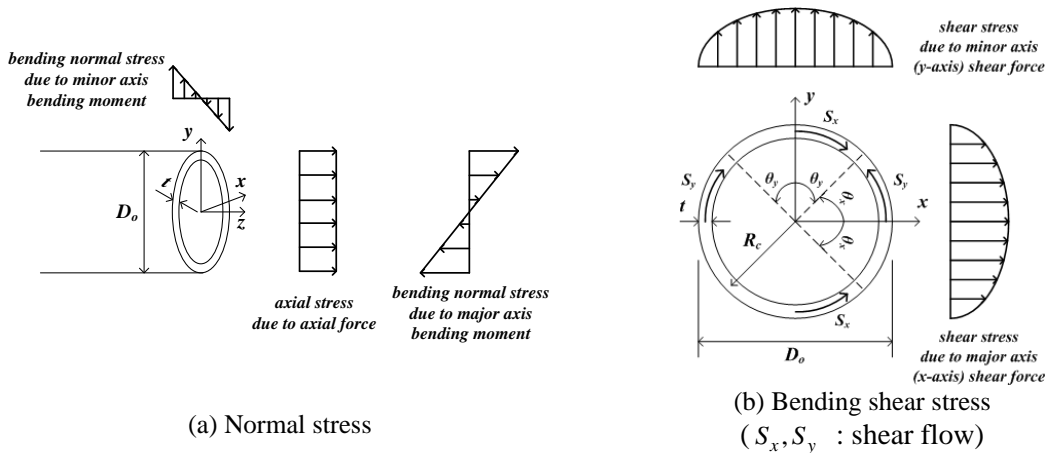


Fig. 16 Stress distribution acting on a section

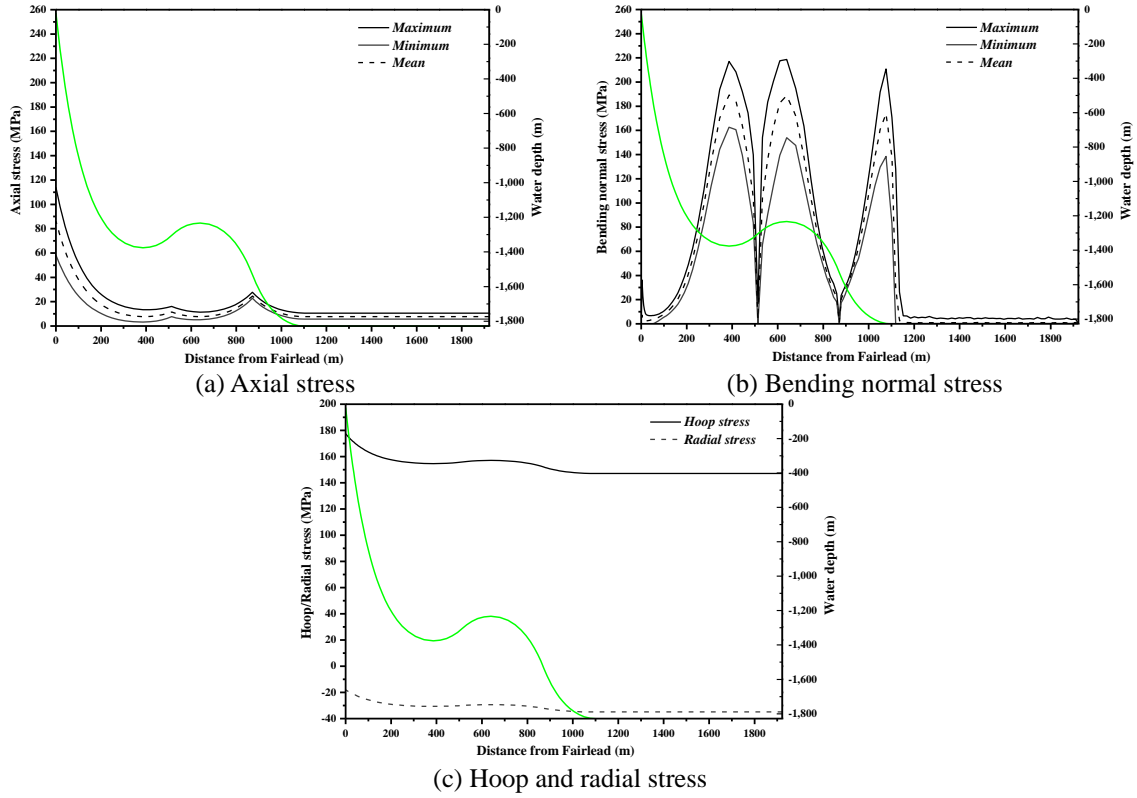


Fig. 17 Stress component and distribution

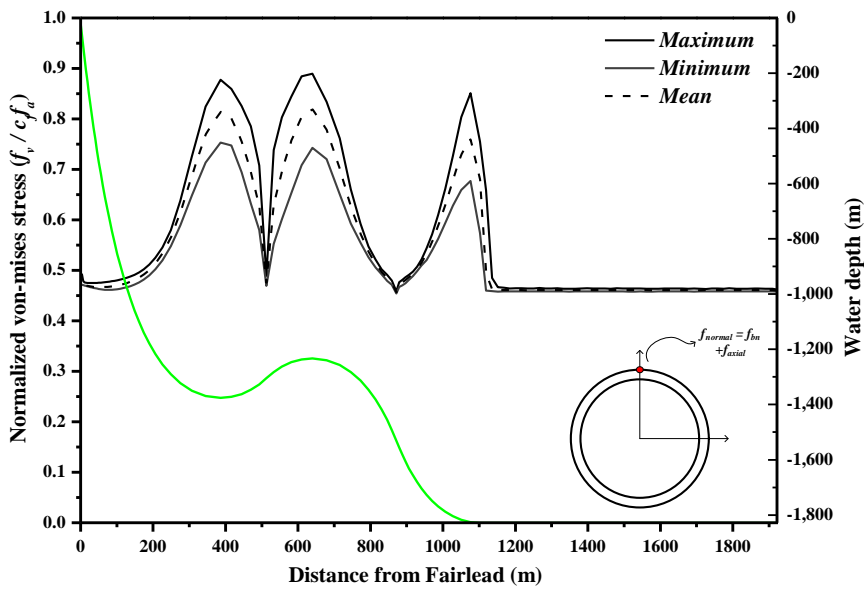


Fig. 18 Von-Mises stress distribution along the LWSCR

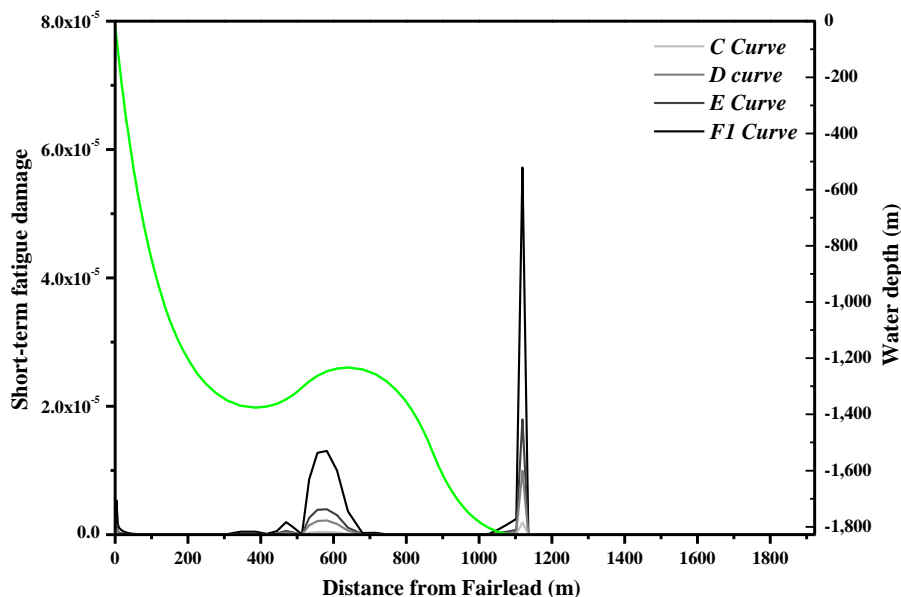


Fig. 19 Short-term fatigue damage index of the LWSCR due to the -hour 100y storm (Max. damage index: $5.72\text{E-}5$ nearby TDP)

As shown in Fig. 17, while maximum bending normal stress occurs at the maximum-curvature portion and maximum axial force happens at hang-off point, the variations of the pressure induced hoop and radial stresses are small along the length ranging $147.08 \sim 177.40$ and $-34.94 \sim -17.97$ MPa, respectively. It means that the pressure induced stresses alone make Von-Mises stress of $167.31 \sim 187.03$ MPa, which is 37.3~41.7 % of the yield stress. For calculating the hoop and radial stresses, maximum internal pressure of 55.16 MPa (8000.0 psi) is assumed. Fig. 18 shows the distribution of the normalized non-dimensional Von-Mises stress, which is calculated by $\sigma_v / C_f C_a f_y$. As shown in the figure, maximum stress level of Von-Mises stress is less than 0.9. It means that every member of the LWSCR does not have the stress level exceeding material limit under the extreme environmental condition.

4.7 Short-term fatigue damage comparison

The Short-term fatigue damage of risers, induced during a particular storm, can be estimated by the Miner's rule. To use the method, the levels and cycles of fluctuating stresses acting on a critical point should firstly be obtained by Rainflow counting method. By using the Rainflow counting method, the mean correction method, and Miner's rule with 4 different S-N curves presented by DNV-RP-F204, the short-term fatigue damages of the LWSCR can be estimated for the given storm condition.

The resulting short-term fatigue damage is not serious compared to that of ordinary SCRs, as shown in Fig. 19. The maximum fatigue damage of the LWSCR occurs near the TDP but its magnitude is still very small. So, LWSCR is also shown to be effective in increasing the riser fatigue life. So far, we investigated the dynamic characteristics and the resulting stresses of a

particular LWSCR profile. Then, we may have the question “what is the most optimal profile of LWSCR for the given FPSO and environment?”. Intuitively, if we have more curvature, the effect of dynamic absorption is increased. However, more curvature results in more flow-assurance problem. Also, we may have the question “Do the location of TDP and length of arch significantly affect the dynamics and stresses?”. To answer those questions, a systematic case study is conducted in the following.

5. Case Study 1: Effect of the initial sag and arch shape on the structural behavior of deepwater LWSCRs

Firstly, the effect of the initial sag and arch shape on the structural behavior of deepwater LWSCRs is investigated based on the previously described numerical simulations. As shown in Fig. 20, three different LWSCRs which have the same TDP location but different initial sag/arch curvatures are designed for LP line #13 and #15 of the FPSO system. By the same coupled dynamic analysis, the motion, internal force, and short-term fatigue damage under the same 100y hurricane event are estimated to assess its effect. In practice, the initial curvature can be controlled by the arrangement of buoys.

As shown in Fig. 21, the vertical velocity along the LWSCR is definitely affected by the initial shape of the sag and arch bend. With larger curvature, maximum vertical velocities near TDP are decreased, which means that more motion-isolation effect is induced with deeper sag and arch bend. The range of TDP is also decreased with larger curvature. Table 7 shows the maximum and minimum vertical velocities at the touchdown catenary of each riser.

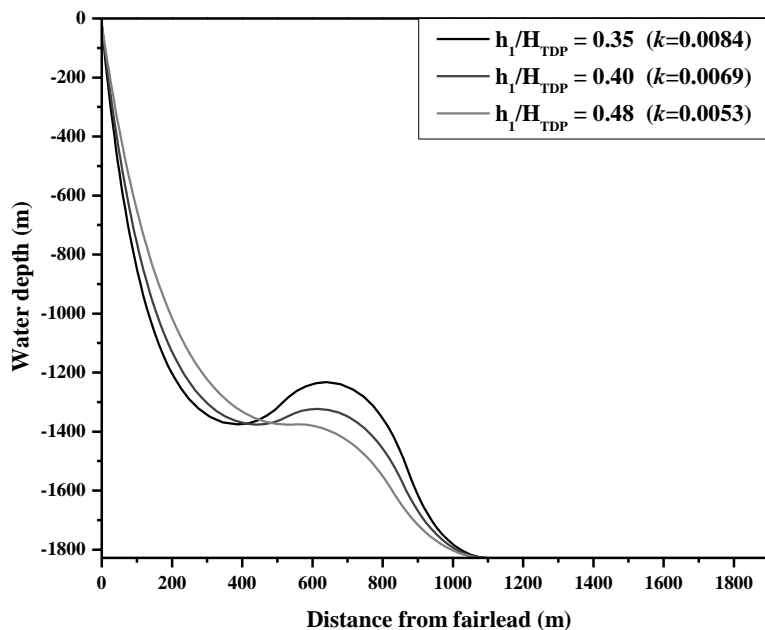


Fig. 20 Initial configuration of the three LWSCRs which have different initial curvatures at the origins of sag and arch, with same TDP ($d_1/D=0.75$, $H_{TDP}/H_{ANCHOR}=0.57$)

Table 7 Maximum and minimum vertical velocities of the compared LWSCRs

Riser configuration	Vertical velocity (m/s)	
	Maximum	Minimum
LWSCR with initial arch and sag curvature of 0.0084	1.390	-1.312
LWSCR with initial arch and sag curvature of 0.0069	2.060	-1.792
LWSCR with initial arch and sag curvature of 0.0053	3.402	-2.725

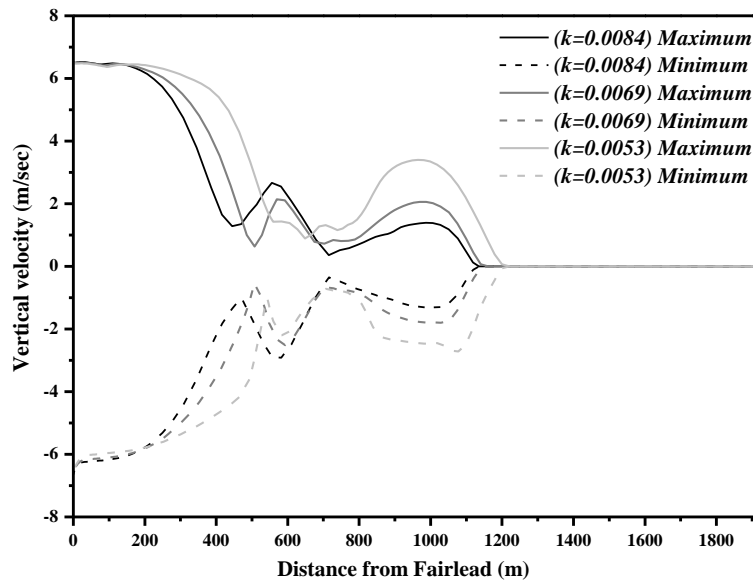


Fig. 21 Vertical velocity distribution of the compared LWSCRs

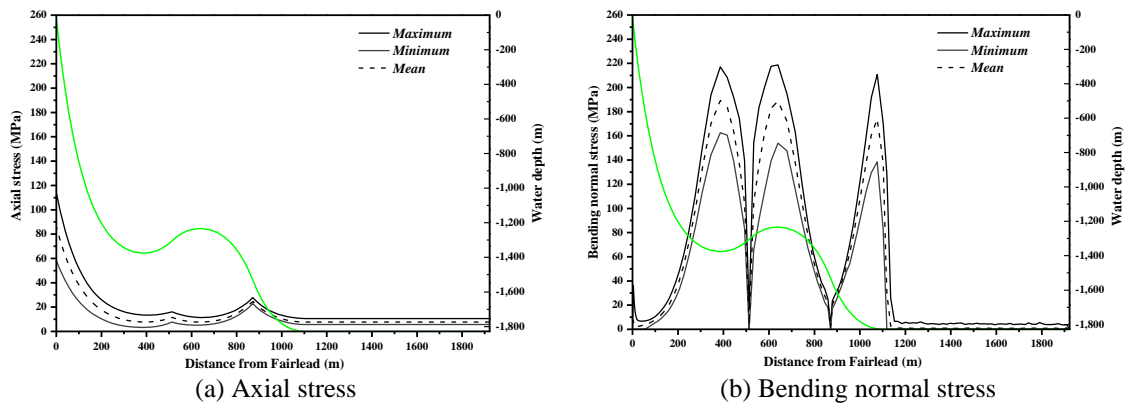
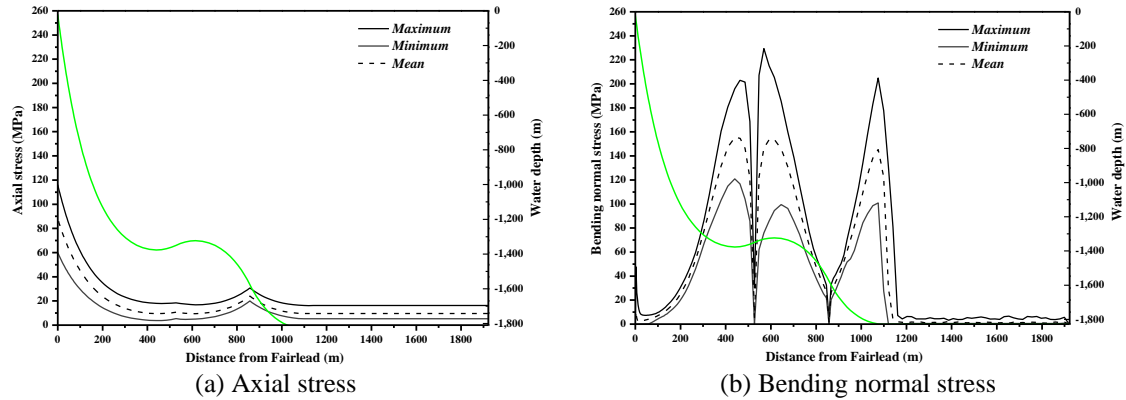
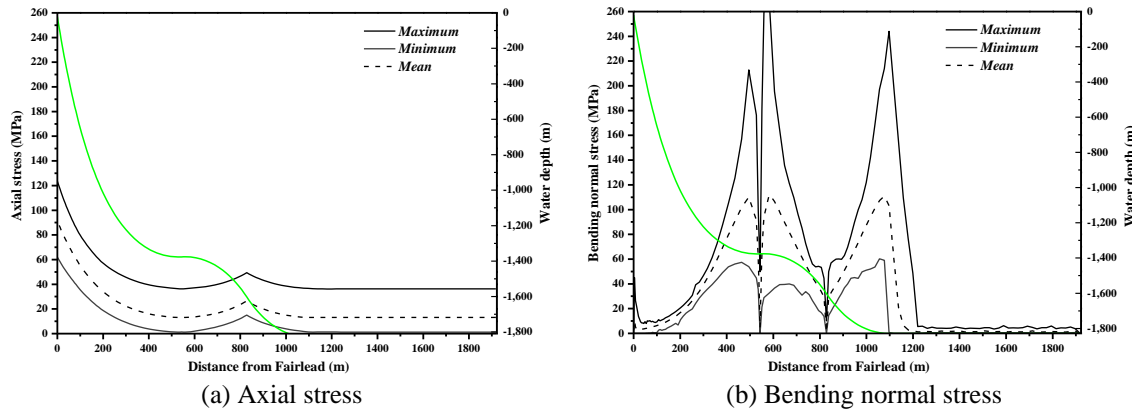
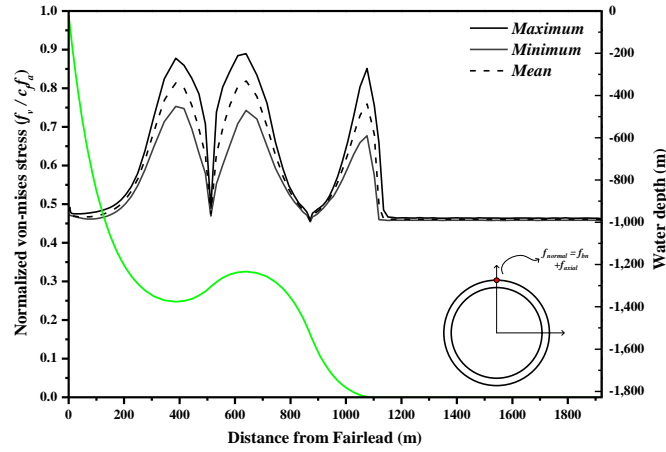


Fig. 22 Normal stress distribution of the LWSCR with $k=0.0084$

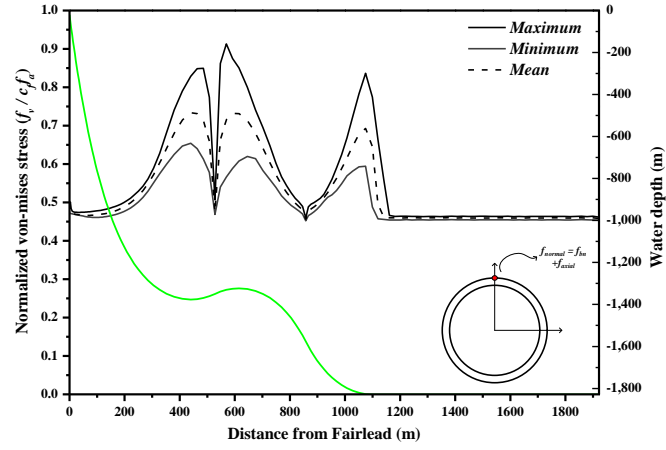
Fig. 23 Normal stress distribution of the LWSCR with $k=0.0069$ Fig. 24 Normal stress distribution of the LWSCR with $k=0.0053$

Figs. 22-24 show the normal-stress distributions of the compared LWSCRs. When considering the bending stress, its mean values increase with increasing initial curvature, as expected. Whereas, dynamic bending stress decreases with increasing initial curvature due to higher velocity-absorption effect. As a result, the total bending stresses increase with decreasing initial curvature. The axial dynamic tensions increase with decreasing curvature due to less motion-absorbing capability. As a result, the minimum axial tensions get closer to zero (or eventually negative value) with the decrease of curvature. As shallow sag and arch is used, the minimum tension is close to zero, which means that there is a potential for negative tension (compressional axial force) near TDP. The negative tension can cause local dynamic buckling as investigated in detail in Kim and Kim (2015). If localized dynamic buckling occurs near TDP, it may cause permanent damage to the structure. (Kim *et al.* 2014)

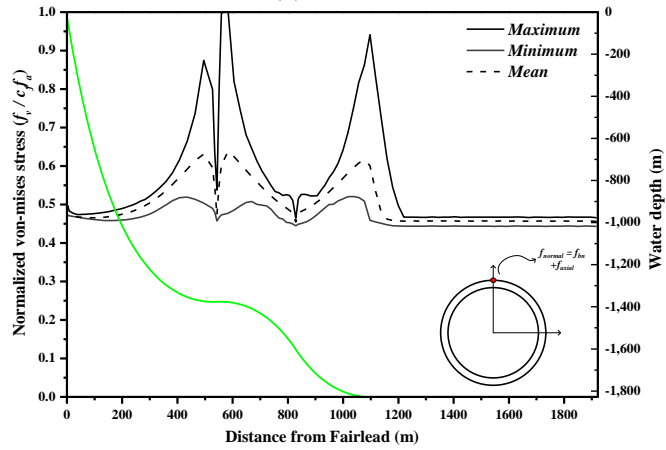
For more initially bent shape, more buoyancy forces by a series of buoys should be applied to wider range and it makes larger initial bending moment but less dynamic bending stresses. More buoys mean higher cost. Also, the larger curvature makes the overall flow assurance worse. Therefore, there should be an optimal curvature of the LWSCR after considering all those factors.



(a) $k=0.0084$



(b) $k=0.0069$



(c) $k=0.0053$

Fig. 25 Normalized Von-Mises stress distribution of the compared LWSCRs

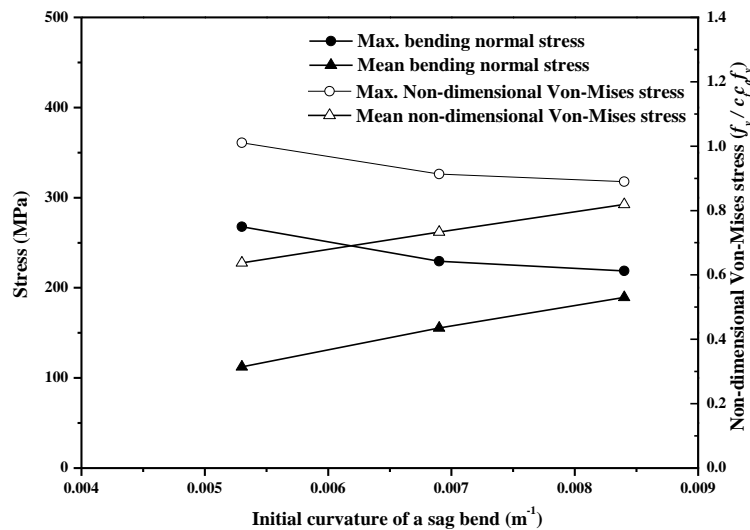
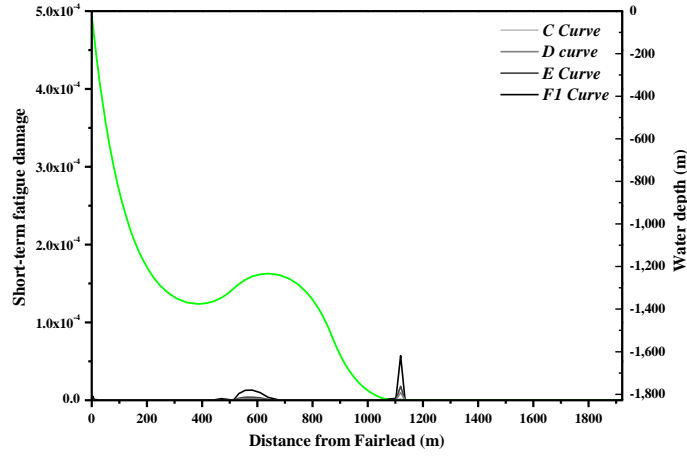


Fig. 26 Structural stress level vs initial curvature of the sag and arch bend

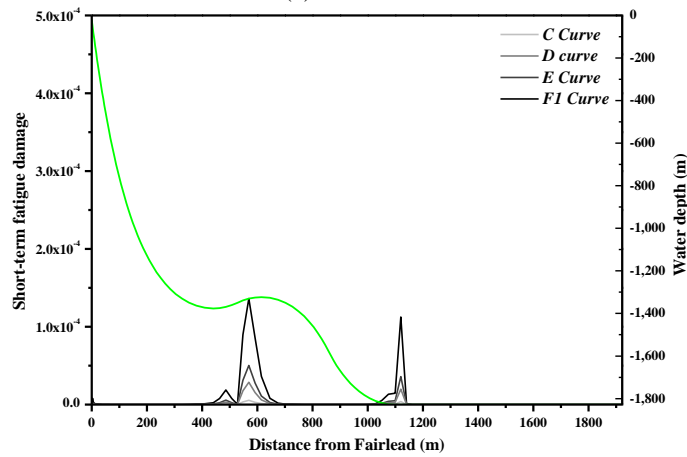
The short-term fatigue damage of each LWSCR is estimated based on the time-series of structural stresses due to the 100y-return-period hurricane for 3-hour. In order to calculate the short-term fatigue damage index, Miner's rule is used considering the S-N curve suggested by DNV-RP-F204. As shown in Fig. 27, short-term fatigue damage under the same environmental condition increases with decreasing initial curvature. The figure also reveals hot spots along the riser for each case. Fatigue is mainly affected by the range and cycles of the fluctuating structural stress. Therefore, the motion isolation effect can effectively mitigate the accumulated fatigue damage. According to the fatigue damage estimation of the LWSCR, the left end of the buoyancy catenary and touchdown point are the most damaged spots. Also, as shallow sag and arch is used, the most damaged part is changed from the TDP to the junction of sag bend and arch bend. The short-term fatigue damage is quite small compared to the conventional SCR of the same case (Kim and Kim 2014).

6. Case Study 2: Effect of the initial TDP location on the structural behavior of deepwater LWSCRs

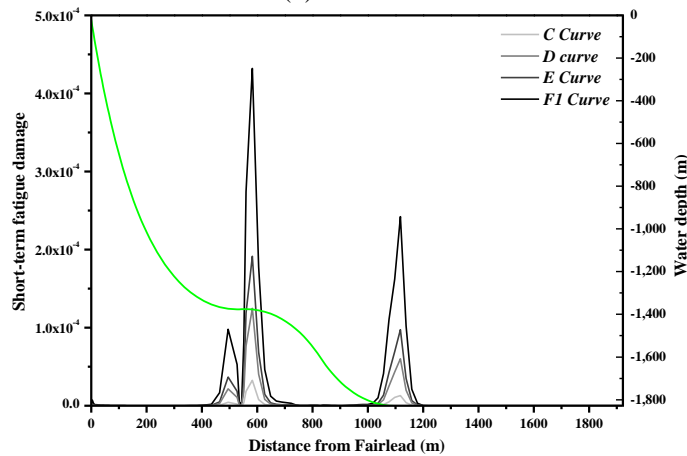
As shown in the previous section, it is obvious that the initial curvature of LWSCR affects the motion isolation effect and deeper arch reduces its dynamic response while causing flow-assurance problem. In this section, the effect of the other LWSCR geometric parameter, the initial position of TDP, on the overall structural behavior is investigated. For this case study, following four individual LWSCRs which have the same h_1/H_{TDP} ratio of 0.35 but different initial TDP locations are used for the LP line #13 and #15 of the same FPSO system.



(a) $k=0.0084$



(b) $k=0.0069$



(c) $k=0.0053$

Fig. 27 Short term fatigue damage index of the compared LWSCRs

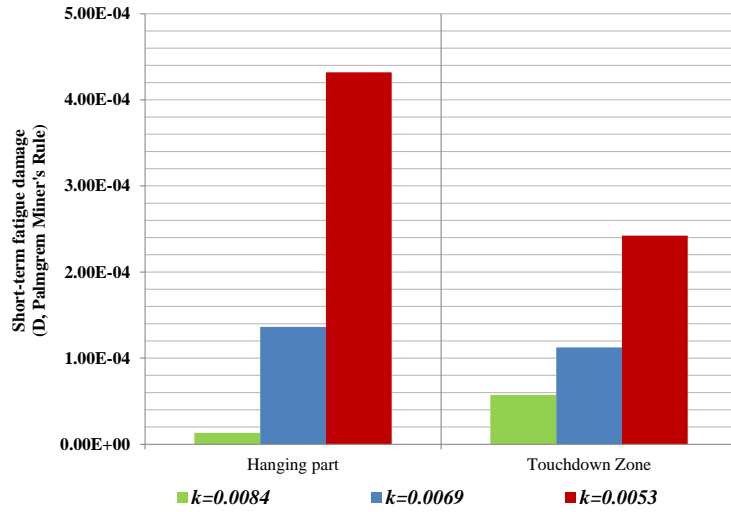


Fig. 28 Short-term fatigue damage index due to the 100y return period hurricane (3-hour duration, DNV F-1 S-N curve used)

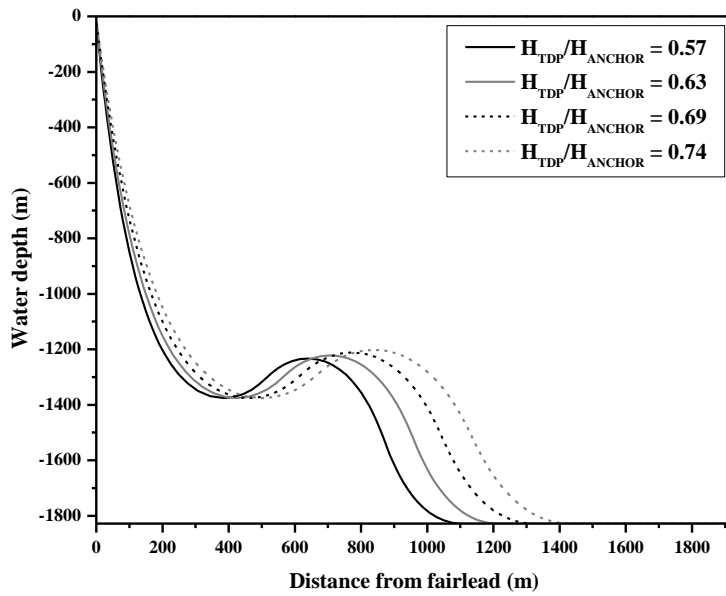


Fig. 29 Initial configuration of the compared LWSCRs which have different initial TDP locations

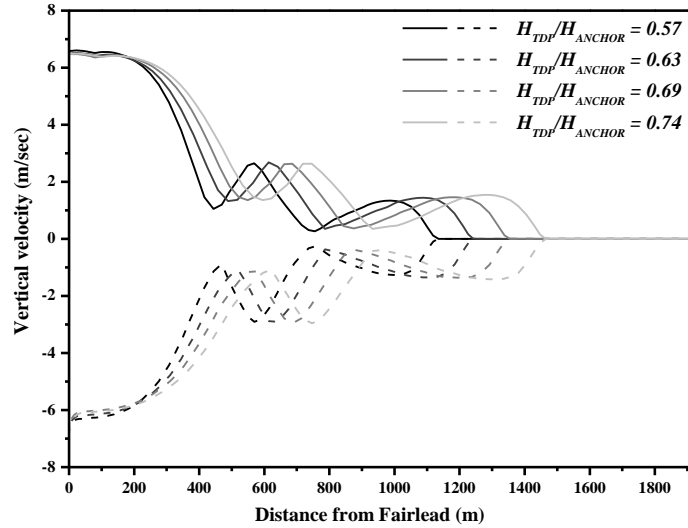


Fig. 30 Vertical velocity distribution of the compared LWSCRs

Fig. 30 shows the maximum and minimum vertical velocities along the riser. As shown in Fig. 30, from the perspective of motion-isolation effect by changing the initial position of TDP, there is little difference among them. So, it can be concluded that the motion-absorption effect of LWSCR is more affected by the initial shape of the sag and arch bend than the initial position of TDP.

Figs. 31-34 show the maximum, mean, and minimum axial stresses and bending stresses. For the axial stress along the riser, there is little difference among them. On the other hand, there is some benefit by placing TDP farther since the maximum bending stresses gradually become smaller. The range of dynamic variation is about the same among the four cases. Therefore, the gradual reduction of the maximum bending stress is caused by that of mean bending stress since the initial curvature is slightly reduced by having farther TDP. Due to little change in the range of dynamic stresses among the four cases, it is expected that there is little difference in fatigue life among them.

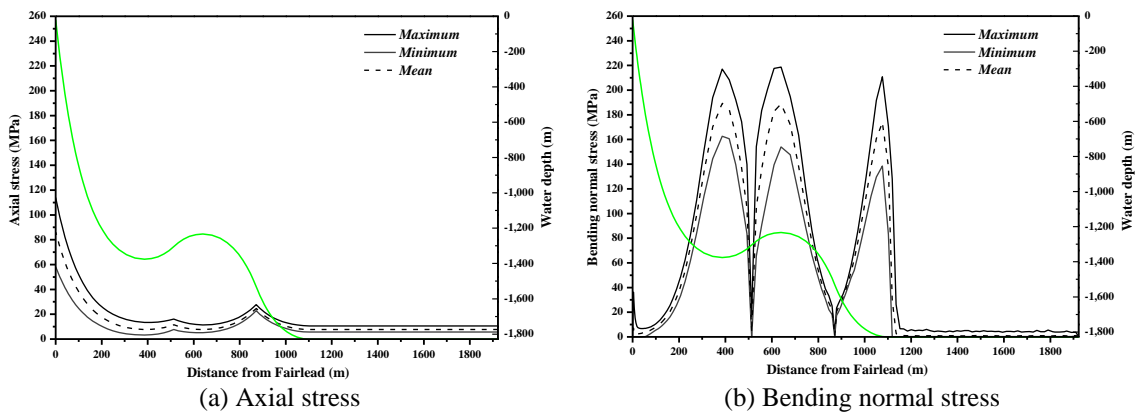


Fig. 31 Normal stress distribution of the LWSCR with $H_{TDP}/H_{ANCHOR}=0.57$

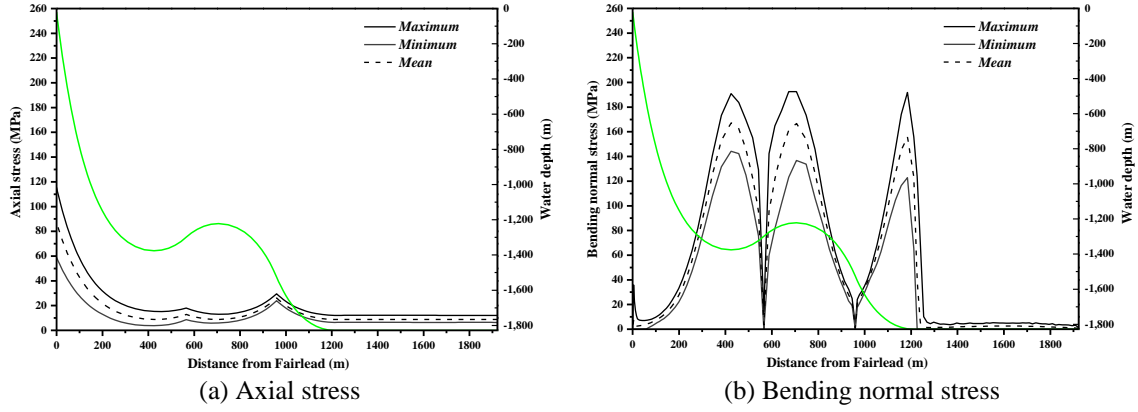


Fig. 32 Normal stress distribution of the LWSCR with $H_{TDP}/H_{ANCHOR}=0.63$

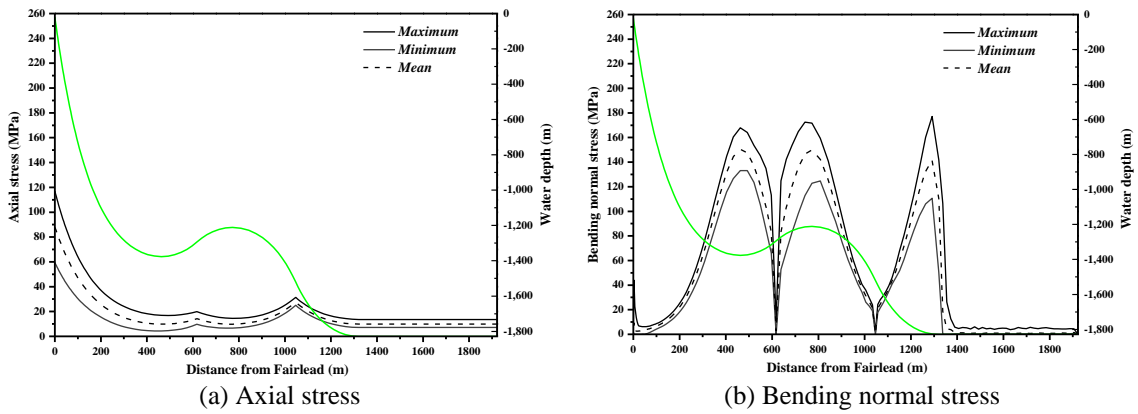


Fig. 33 Normal stress distribution of the LWSCR with $H_{TDP}/H_{ANCHOR}=0.69$

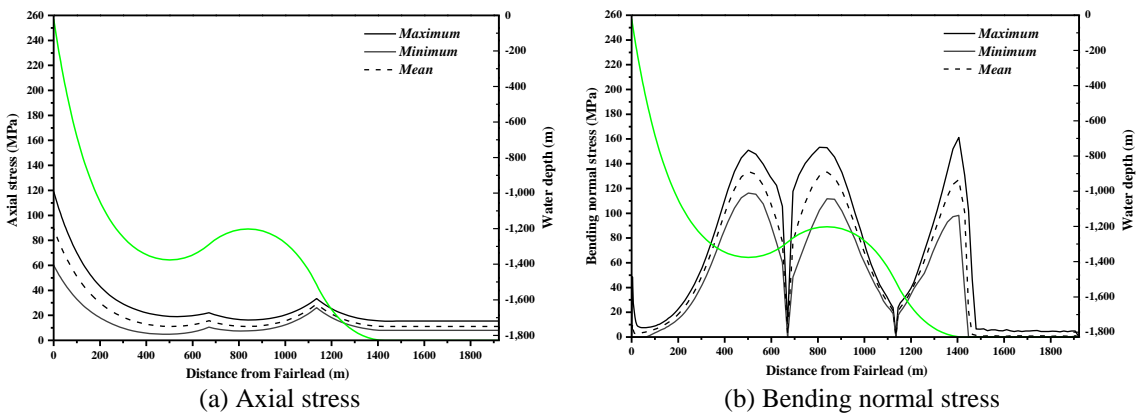
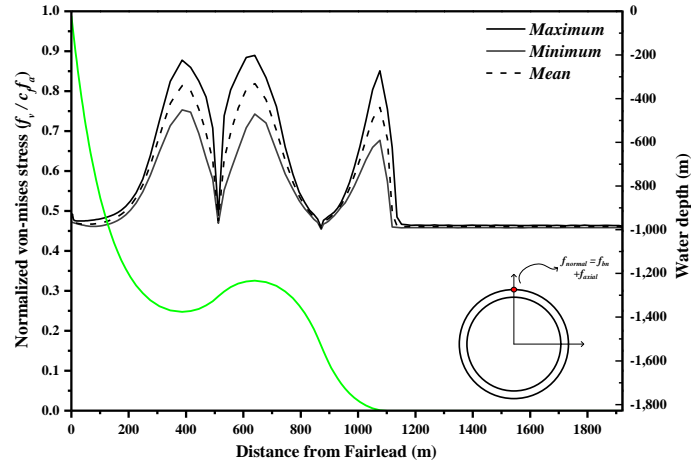
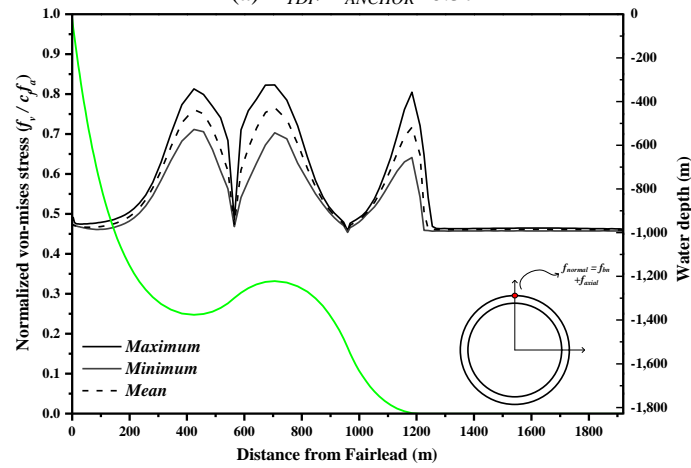


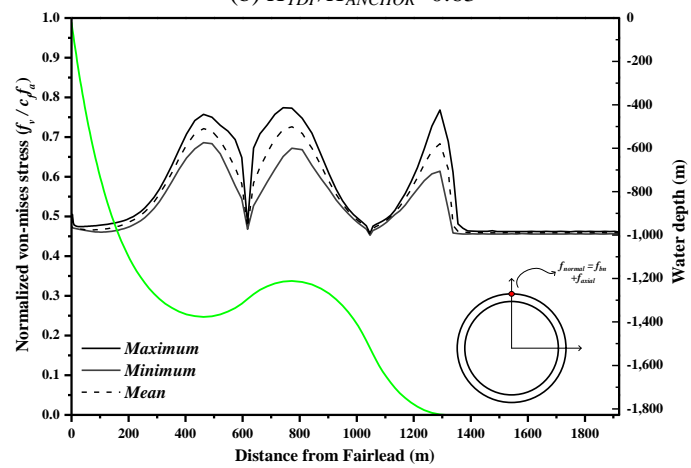
Fig. 34 Normal stress distribution of the LWSCR with $H_{TDP}/H_{ANCHOR}=0.74$



(a) $H_{TDP}/H_{ANCHOR}=0.57$



(b) $H_{TDP}/H_{ANCHOR}=0.63$



(c) $H_{TDP}/H_{ANCHOR}=0.69$

Continued-

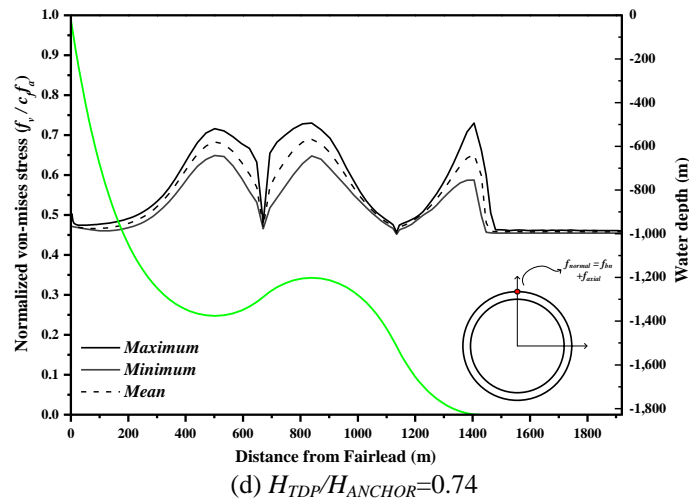


Fig. 35 Normalized Von-Mises stress distribution of the compared LWSCRs

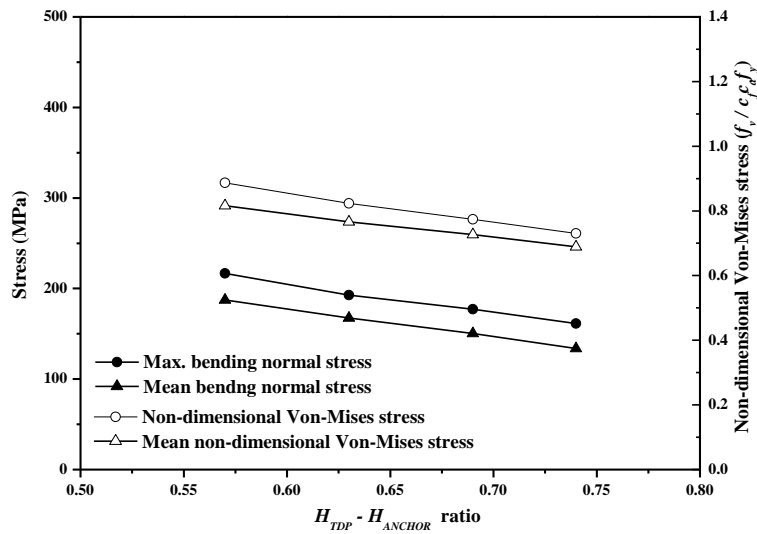


Fig. 36 Structural stress level vs initial position of TDP

Fig. 35 shows the corresponding comparison of the Von-Mises (total) stresses among the four cases. Since there is little change in axial stresses, the trend of total stress generally follows that of bending stresses. This can be more clearly seen in Fig. 36 i.e., Von-Mises stresses gradually decrease with increasing the TDP distance. However, the benefit should be weighed against the anticipated cost increase by having farther TDP.

7. Conclusions

In this study, the effects of the geometric parameters of LWSCRs on its dynamic behavior and resulting stresses are investigated for a turret-moored FPSO under the 100-yr hurricane condition in the GOM. The global performance evaluation of the system is evaluated by the time-domain floater-mooring-riser fully-coupled dynamics simulation program developed by authors. According to the case study, changing initial TDP location while fixing the initial bent shape only affects the mean bending stresses. On the other hand, changing curvature while fixing the TDP location affects both mean and dynamic bending stresses. Larger curvature reduces dynamic responses but can cause more trouble for flow assurance. Reducing the range of dynamic stresses is helpful in increasing fatigue life of hot-spots. Also, more buoyancy modules to have larger curvature mean higher cost. The benefit of having farther TDP location is marginal considering the corresponding increase of cost. With farther TDP position, only the mean total stresses are decreased with little change in dynamic stresses. In conclusion, an optimal initial profile of LWSCR for any given floating system can be determined through this kind of systematic comparison-by-simulation study.

Acknowledgements

This research was supported by Basic Science Research Program through the National Research Foundation of Korea (NRF) funded by the Ministry of Education (2016R1D1A1A02937083) and KAIST Smart Submerged Floating Tunnel ERC Program through the NRF funded by the Ministry of Science and ICT (2017R1A5A1014883).

References

- API 2INT-MET (2007), Interim guidance on hurricane conditions in the Gulf of Mexico, American Petroleum Institute; Washington, D. C., U.S.A
- API RP 2RD (2009), Design of risers for floating production systems (FPSs) and tension-leg platforms (TLPs), American Petroleum Institute; Washington, D. C., U.S.A
- Garrett, D.L. (1982), "Dynamic analysis of slender rods", *J. Energ. Resour. Technol.*, **104**(4), 302-307.
- Jacob, B.P., Reyes, M.C.T., Lima, B.S.L.P., Torres, A.L.F.L., Mourelle, M.M. and Silva, R.M.C. (1999), "Alternative configurations for steel catenary risers for turret moored FPSO's", *Proceedings of the 9th International Offshore and Polar Engineering Conference*, Brest, May.
- Kang, H.Y. and Kim, M.H. (2012), "Hydrodynamic interactions and coupled dynamics between a container ship and multiple mobile harbors", *Ocean Syst. Eng.*, **2**(3), 217-228.
- Kim, M.H., Koo, B.J., Mercier, R.M. and Ward, E.G. (2005), "Vessel/mooring/riser coupled dynamic analysis of a turret-moored FPSO compared with OTRC experiment", *Ocean Eng.*, **32**, 1780-1802
- Kim, S., Kim, M.H., Shim, S. and Im, S. (2014), "Structural performance of deepwater lazy-wave steel catenary risers for FPSOs", *Proceedings of the 24th International Offshore and Polar Engineering Conference*, Busan, May.
- Kim, S. and Kim, M.H. (2015), "Dynamic behaviors of conventional SCR and Lazy-Wave SCR for FPSOs in deepwater", *Ocean Eng.*, **106**, 396-414.
- Kuiper, G.L., Brugmans, J. and Metrikine, A.V. (2008), "Destabilization of deep-water risers by a heaving platform", *J Sound Vib.*, **310**, 541-557.
- Li, S. and Nguyen, C. (2010), "Dynamic response of deepwater lazy-wave catenary riser", *Deep Offshore*

- Technology International*, Amsterdam, December.
- Ran, Z. (2000), "Coupled dynamic analysis of floating structures in waves and currents", Ph.D. Dissertation, Texas A&M University, College Station, TX, USA.
- Ran, Z. and Kim, M.H. (1997), "Nonlinear coupled responses of a tethered spar platform in waves", *Int. J. Offshore Polar.*, **7**(2), 111-118.
- Silva, R.M.C., Moraes, M.G.G., Cristisinelis, A.F. and Torres, A.L.F.L.T (1999), "The feasibility study and preliminary design of a steel riser attached to a FPSO", *Proceedings of the 18th International Conference on Offshore Mechanics and Arctic Engineering*, St. John's Newfoundland, July.
- Tahar, A. and Kim, M.H. (2003), "Hull/mooring/riser coupled dynamic analysis and sensitivity study of a tanker-based FPSO", *Appl. Ocean Res.*, **25**, 367-382.
- Torres, A.L.F.L., Mourelle, M.M. and Silva, R.M.C. (2001), "Fatigue damage verification of steel catenary risers", *Proceedings of the 20th International Conference on Offshore Mechanics and Arctic Engineering*, Rio de Janeiro, June.
- Torres, A.L.F.L., Casaprima, E.G., Queija, M.S., Dantas, C.M.S., Mourelle, M.M. and Silva, R.M.C. (2002), "Lazy-wave steel rigid risers for turret-moored FPSO", *Proceedings of the 21th International Conference on Offshore Mechanics and Arctic Engineering*, Oslo, June.
- Torres, A.L.F.L., Gonzalez, E.C., Ferreira, M.D.S., Siqueira, M.Q., Mourelle, M.M. and Silva, R.M.C. (2003), "Lazy-wave steel rigid risers for FSO with spread mooring anchoring system", *Proceedings of the 22th International Conference on Offshore Mechanics and Arctic Engineering*, Cancun, June.
- Yang, C.K. and Kim, M.H. (2010), "Linear and nonlinear approach of hydropneumatic tensioner modeling for spar global performance", *J. Offshore Mech. Arct.*, **132**(1), 011601.
- Yang, C.K. and Kim, M.H. (2011), "The structural safety assessment of a tie-down system on a tension leg platform during hurricane events", *Ocean Syst. Eng.*, **1**(4), 263-283.
- Yang, H. and Li, H. (2011), "Sensitivity analysis of fatigue life prediction for deepwater steel lazy wave catenary risers", *Sci. China Technol. Sc.*, **54**(7), 1881-1887.
- Yue, B., Campbell, M., Walters, D., Thompson, H. and Raghavan, K. (2010), "Improved SCR design for dynamic vessel application", *Proceedings of the 29th International Conference on Ocean, Offshore and Arctic Engineering*, Shanghai, June.
- Yue, B., Walters, D., Yu, W., Raghavan, K. and Thompson, H. (2011), "Lazy wave SCR on turret moored FPSO", *Proceedings of the 21th International Offshore and Polar Engineering Conference*, Maui, June.
- Wu, M. and Huang, K. (2007), "The comparison of various SCR configurations for bow turret moored FPSO in West Africa", *Proceedings of the 16th International Offshore and Polar Engineering Conference*, San Francisco, May.